SECONDARY PHASE FORMATION DURING NUCLEAR WASTE-GLASS DISSOLUTION

T. A. Abrajano,[1] J. K. Bates,[1] A. B. Woodland,[1]
J. P. Bradley,[2] and W. L. Bourcier[3]

[1] Argonne National Laboratory, 9700 South Cass Avenue, Argonne, Illinois 60439

[2] McCrone Associates, Inc., 850 Pasquinelli Drive, Westmont, Illinois 60559

[3] Lawrence Livermore National Laboratory, Yucca Mountain Project
P.O. Box 5514, Livermore, California 94551

Abstract—Secondary minerals formed during simulated weathering of nuclear waste glasses have been identified by analytical electron microscopy. A complete description of the reacted glass, from the outermost surface in direct contact with the leachant solution to the reacting front that migrates into the bulk glass, was obtained. Manganese and iron oxyhydroxide phases and saponite were found to have precipitated onto the residual glass surface from the leachant solution. Iron-bearing smectite, serpentine, and manganese and uranium-titanium oxyhydroxides formed *in situ* in the glass in several distinct bands at different depths beneath the original surface. This sequential development of secondary phases displays a clear trend toward more order and crystallinity in the phases farthest from the reaction front and indicates that complete restructuring of the glass into crystalline phases did not occur at the interface with fresh glass. Additionally, the formation of a discrete uranium-bearing phase, as opposed to uranium uptake by precipitated phases, suggests that stable actinide phase formation rather than ion exchange may be a possible mechanism for retarding radionuclide release to the environment.

Key Words—Dissolution, Glass, Hydration, Manganese oxide, Nuclear waste, Serpentine, Smectite, Uranium.

INTRODUCTION

The disposal of high-level nuclear waste is a unique environmental problem in that it requires a solution that remains technically valid on geological time scales (10^2–10^5 years). One proposed disposal method is to incorporate radionuclides into borosilicate glass followed by burial in an underground repository. Glasses are attractive candidates for waste disposal because of their ability to accept radionuclides. Before glasses can be used for disposal, however, their leaching characteristics must be evaluated and modeled (DOE, 1989).

Glass is a metastable solid, which, given enough time in a reactive aqueous environment, will transform into a thermodynamically stable assemblage of secondary phases (Mendel, 1984; Grambow, 1985; Abrajano *et al.*, 1988; Bourcier, 1989). Because these phases control the concentrations of all elements released to the aqueous phase during glass reaction, their identification is vital to understanding the long-term stability of glasses in a repository environment. Based on the sequence of phase formation and a description of the reacted glass structure as derived from simple experimental systems, a mechanism of glass reaction can be postulated and can then be used to develop a predictive model of the long-term glass behavior. The development of such a model has been difficult, however, because the detailed structure of reacted waste glass has not been known. The secondary reaction products formed on experimentally reacted waste glasses are often

fragile, poorly crystalline, ultrathin (1–20 μm) coatings, which make sample preparation and analysis difficult (Murakami *et al.*, 1989; Abrajano *et al.*, 1989; Lutze *et al.*, 1983; Godon *et al.*, 1988). As a result, most researchers have only been able to speculate on the identity of secondary phases or the reaction mechanism.

In the present work, analytical electron microscopy (AEM) was used to identify the secondary phases that formed during the reaction of simulated nuclear-waste glass with water at 90°C. Use of AEM was successful because, for the first time, electron-transparent thin sections of the fragile layers were prepared with minimal disturbance of their microstructures and textures. A complete description was made of the reacted glass, from the outermost surface in direct contact with the leachant solution to the reacting front that migrated into the bulk glass. In addition, glasses with and without uranium were examined to assess radionuclide-release behavior. These observations have significantly advanced our understanding of glass stability in a geologic repository for nuclear wastes and have provided new insight into the potential of glass as a medium for the long-term storage of nuclear wastes.

EXPERIMENTAL

Two simulated nuclear-waste glasses, henceforth referred to as glasses I and II (Table 1), were examined. Both glasses were made from the same nominal starting frit, but glass II was modified by adding the waste

Table 1. Initial waste glass compositions.[1]

Oxide	Weight percentage	
	Glass I	Glass II
Li_2O	3.9	4.1
B_2O_3	10.4	10.8
Na_2O	13.3	9.6
MgO_2	1.4	1.4
Al_2O_3	3.4	5.4
SiO_2	42.7	45.8
CaO	1.2	1.0
TiO_2	0.8	0.7
MnO_2	3.7	4.1
Fe_2O_3	13.9	13.2
NiO	1.6	1.5
ZrO_2	0.4	0.4
La_2O_3	0.3	0.4
U_3O_8	—	1.0
Cs_2O	—	0.1
SrO	—	0.1
Others[2]	2.1	—

[1] Glass analyzed by acid and fusion dissolutions followed by inductively coupled plasma spectroscopy.
[2] Others include Cr, Zn, Mo, Ba, Ce, Nd.
Dashes indicate none present.

elements U, Cs, and Sr. The study concentrated on glass I, but glass II was examined to monitor the distribution of U. Both glasses were reacted in batch experiments in deionized water at 90°C (Wicks *et al.*, 1986; Bates *et al.*, 1983) following standard leach testing procedures (Slate, 1985). The leachates (i.e., the solution resulting from glass-water reaction) were analyzed, and samples of glass I reacted for 14, 28, 195, and 546 days (referred to as 14D, 28D, etc.) and glass II (1280D) were examined with scanning electron microscopy (SEM) and AEM. Some samples were also analyzed by X-ray powder diffraction (XRD), infrared (IR) spectroscopy, electron microprobe analysis (EMPA), and secondary-ion mass spectroscopy (SIMS) combined with ion microprobe imaging (IMI).

The AEM thin sections were prepared by using an ultramicrotome equipped with a diamond knife and a procedure developed specifically for preparing micrometer-size geochemical specimens for electron microscopic studies (Bradley, 1988). This procedure permits direct high-resolution observation of grain boundaries and interfaces (Bradley *et al.*, 1989; Bradley and Brownlee, 1989), and enabled electron transparent sections (500–1000 Å thick) of the reacted glass to be prepared with minimal disturbance of their microstructures and indigenous petrography. The thin sections were examined in a 200-keV analytical electron microscope by using lattice-fringe imaging, electron microdiffraction, and quantitative thin-film X-ray analysis (Cliff and Lorimer, 1975; Sheridan, 1989). The accuracy of the X-ray analysis was determined from glass and mineral thin-film standards to be on the order
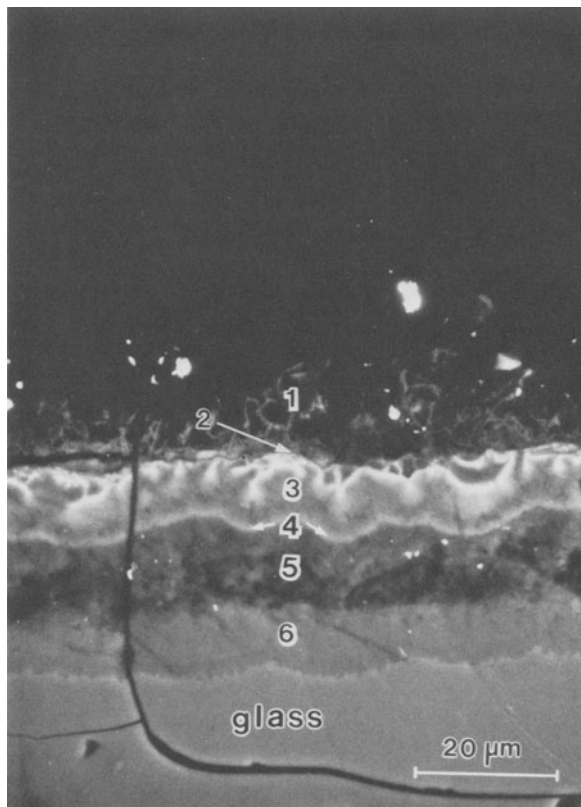

Figure 1. Backscattered electron image of polished, thick, flat specimen of glass 546D showing the reacted zone. Six bands (numbered 1 to 6) can be viewed directly, except for band 2, which is too thin to be resolved in this image (see Figure 3).

of ±5% relative error for major elements and ±30% for minor elements, e.g., Ti and Ca. The acquisition of compositional and structural AEM data was complicated by the overall poor crystallinity within the reacted glass, the fine-scale intercalation of phases, and the sensitivity of some reaction products to electron irradiation damage. A liquid-nitrogen-cooled cold stage was used to minimize irradiation damage and specimen contamination from the microscope itself.

RESULTS

Glass I

After leaching, the glass monoliths were invariably covered with a thin (<50 μm) alteration rind. The rind became thicker with the duration of the experiment and is clearly visible in the backscattered electron image of a cross-section sample of glass I shown in Figure 1. At least six distinct bands were noted within the rind, based on contrasting density differences that are proportional to the backscattered electron intensity. These bands are stacked nearly parallel to the original
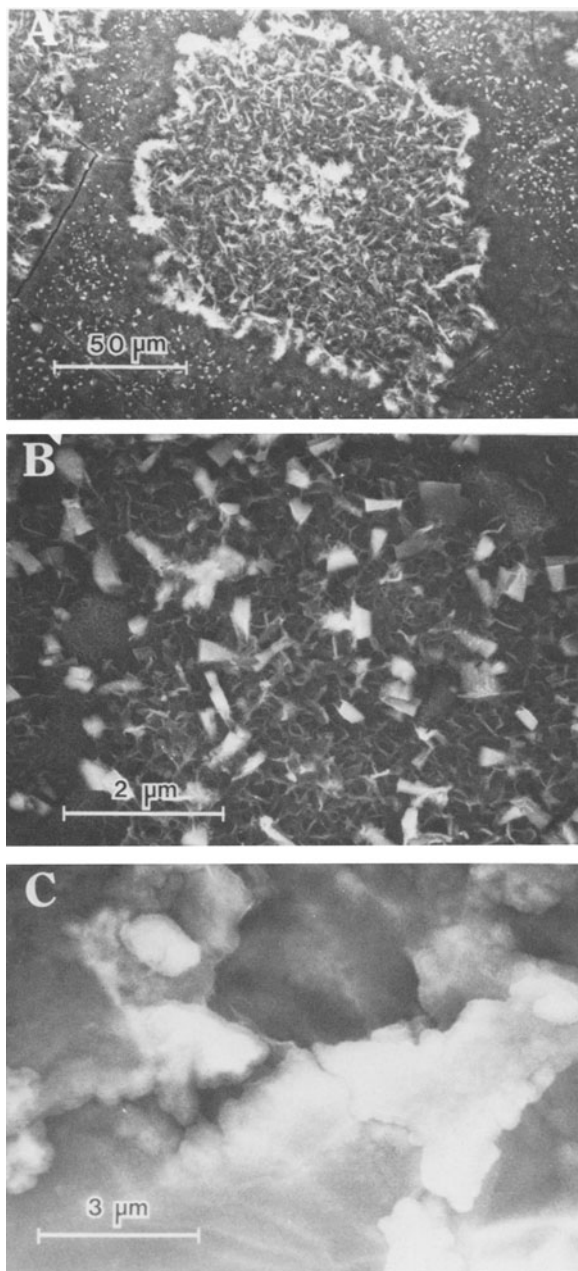
Figure 2. Secondary electron image of the reacted surface of sample 546D. The island/inter-island structure is shown in (A); the distribution of birnessite crystals on the smectite base is shown in (B). Note that the smectite base is free of birnessite crystals in regions adjacent to island features. Regions of iron-rich segregation of Fe_3O_4 and iron metal are present, as identified by backscattered electron imaging in (C).

glass surface; they present a layered appearance and are identified as bands 1–6 in Figure 1. Band 5, which appears darkest in Figure 1, has the lowest electron density and locally shows large cracks perpendicular to the surface. Band 3 is penetrated by bright, high-electron-density fingers, which follow fractures in the unreacted glass surface. Locally, the interface between bands is sharp, even on a nanometer scale (e.g., the band 6–bulk glass interface, the band 2–band 3 interface), whereas the other interfaces are marked by a more gradual change in appearance.

Sample 546D was the most thoroughly studied sample, and samples 14D, 28D, and 195D were examined to elucidate the temporal development of the alteration rind. For example, all six bands were noted in samples 195D and 546D, but bands 4 and 6 were absent in samples 14D and 28D.

Band 1. Band 1 is the outermost band; it is most extensively developed in samples 195D and 546D. The surface of sample 546D is shown in Figure 2; here, a typical "island" and "inter-island" structure is clearly indicated. The intergrowth of at least two phases is also apparent in the high-resolution micrographs (Figures 3 and 4) that were used in phase identification. The phases were identified by lattice-fringe imaging, electron diffraction, and quantitative thin-film analysis. Band 1 consists of elevated "islands" of submicrometer-size birnessite and intertwining fibrous smectite crystals, together with inter-island regions of birnessite, which have formed on a smectite base (band 2).

Four different birnessite morphologies were observed: polycrystalline aggregates, wedges, sheets, and discs (Figure 4). All four exhibit (001) basal spacings of about 7 Å. In the discs, the basal fringes are arranged concentrically about a hollow core. Selected-area electron diffraction (SAED) patterns of individual crystals (Figure 4) gave lattice constants consistent with those reported previously for birnessite (Golden *et al.,* 1986; Giovanoli *et al.,* 1970). The wedge-shaped crystals were concentrated in inter-island regions between the smectite-birnessite islands. Some of these crystals were carefully peeled from the surface of sample 546D and were mounted in a Guinier camera for XRD analysis. These analyses were made to confirm the identification and to evaluate whether birnessite, which contains mixed-valence Mn, was modified in the electron beam during SAED analysis. The measured basal spacings and their relative intensities (Table 2) match XRD results obtained from synthetic birnessite (Chen *et al.,* 1986).

→

Figure 3.   (A) Bright-field transmitted image of an ultramicrotomed thin section of sample 14D showing formation of band 2 on the surface of the glass and in cracks penetrating the original glass surface. (B) Bright-field transmitted image of an ultramicrotomed thin section (500 Å thick) of sample 546D showing band 2 and segments of bands 1 and 3. Band 1 is a mixture of saponite and birnessite, band 2 is mostly vertically oriented fibrous saponite with minor birnessite, and band 3 is an ultra-fine-grained mixture of smectite, serpentine, and possibly birnessite. The inset is a lattice-fringe image of a region of band 2 showing ~15-Å saponite basal spacings.
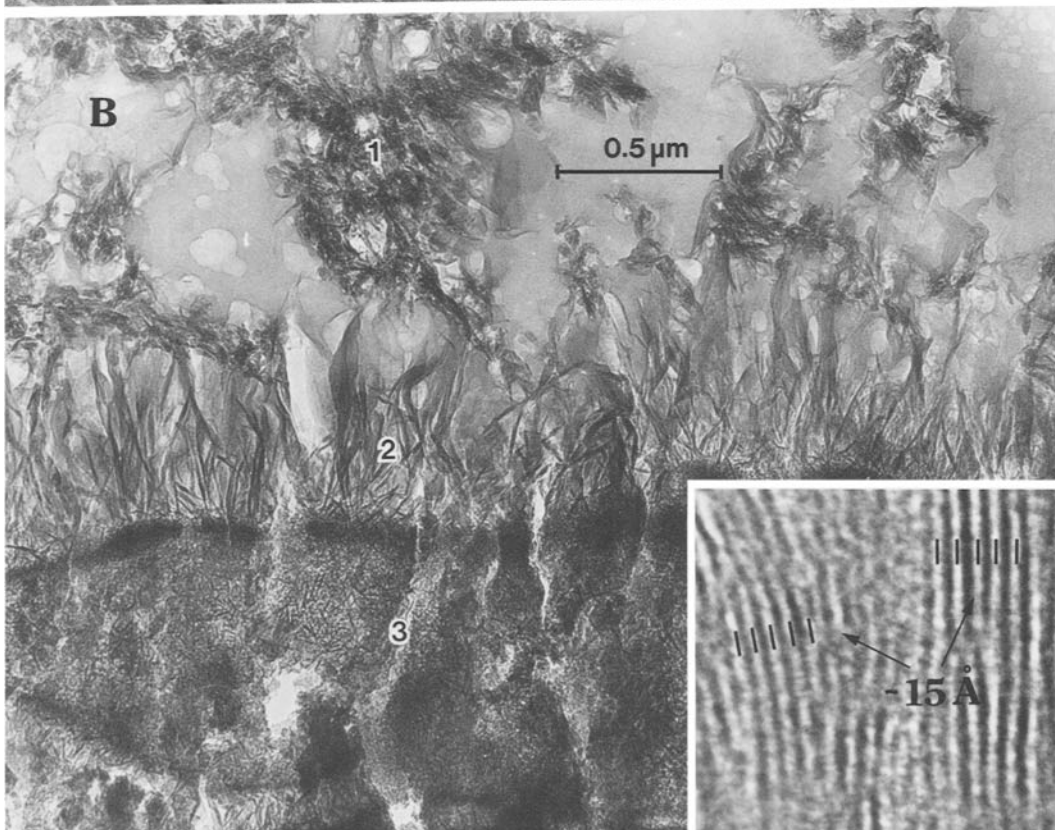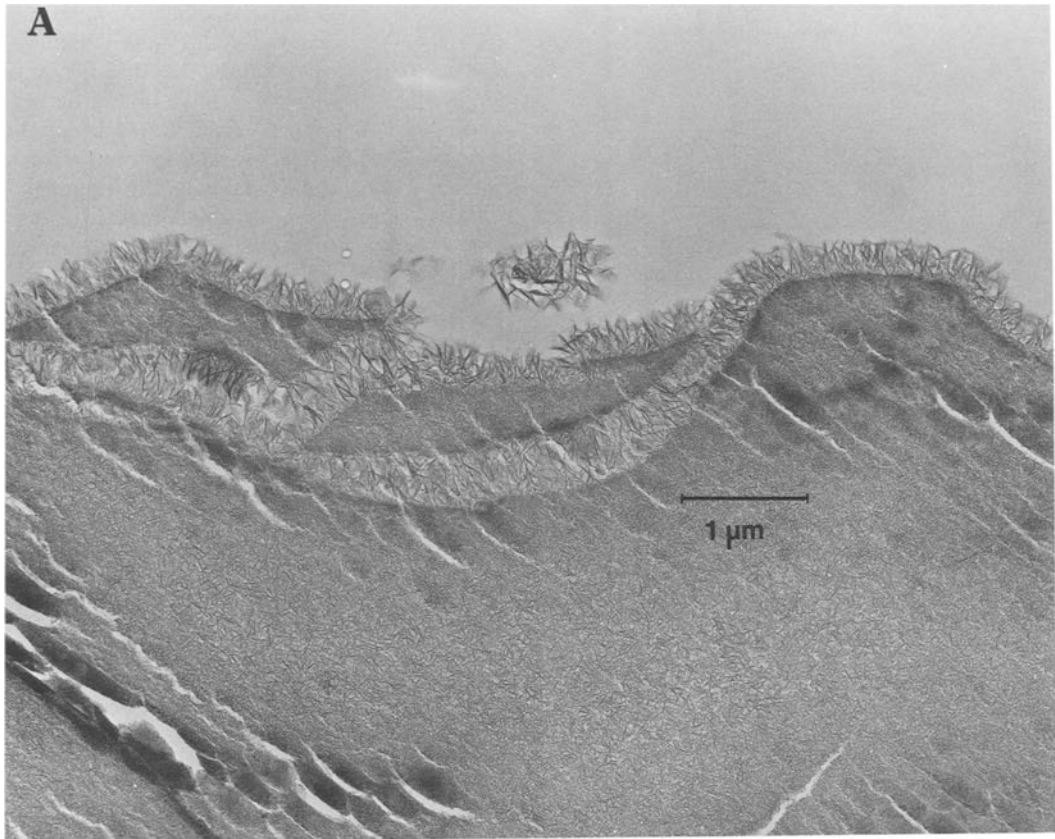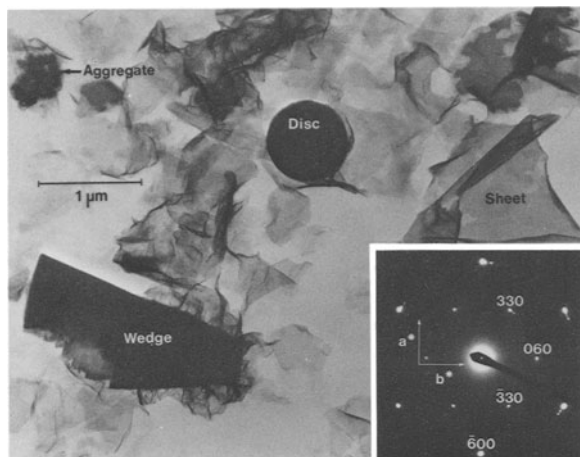
Figure 4. Bright-field electron micrograph of birnessite crystals replicated from the surface of sample 546D. The inset (lower right) is a [001] zone axis selected-area electron diffraction pattern obtained from a birnessite wedge. This pattern is indexed in terms of an orthorhombic unit cell with lattice parameters $a_0 = 8.54$, $b_0 = 15.89$, and $c_0 = 14.26$ Å (Golden et al., 1986).

Birnessite, a manganese oxyhydroxide, is capable of incorporating a wide variety of cations (Golden et al., 1986; Chen et al., 1986; Giovanoli et al., 1970). The composition of birnessite was determined by EMPA analysis of crystals peeled from the inter-island region of sample 546D. The crystals were cleanly removed from the surface and were not intermixed with smectite. Most of the birnessite found in band 1 contains both Ni and Ba in atom proportions Mn:Ni:Ba $\simeq$ 25: 4:1. A few pure Mn-birnessite crystals ($Mn_7O_{13} \cdot 5H_2O$) were also identified. These data correspond well with those obtained on synthetically prepared birnessite, which strongly partitioned Ni and Ba into its structure (Golden et al., 1986).

The island structure of band 1 covers >60% of the surface of samples 195D and 546D; however, it is less well developed in samples 14D and 28D. In sample 14D, band 1 is absent over wide regions of the surface (Figure 3A), but in sample 28D it forms an almost continuous sheet (<0.5 μm thick) rather than the islands and inter-island structure typical of samples 195D and 546D. A Ba-free, Mn-Ni-birnessite is the major component of band 1 for samples 14D and 28D; its
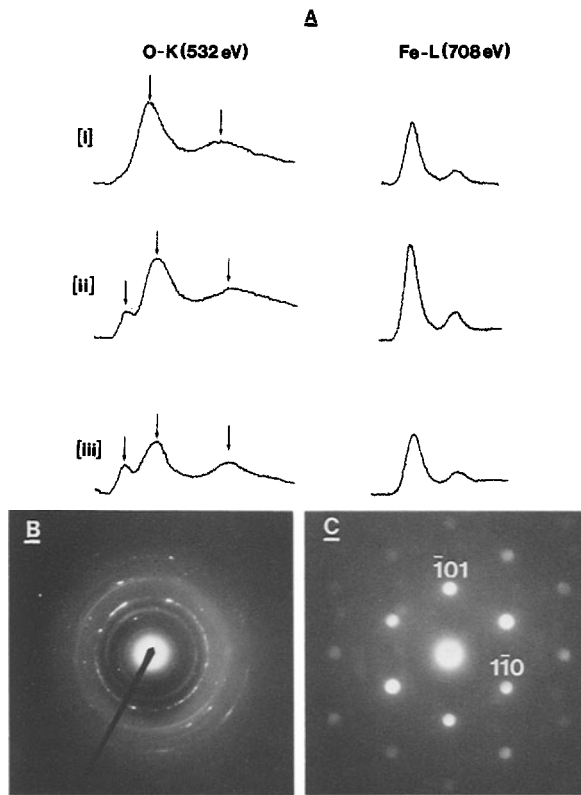

Figure 5. (A) Oxygen-K (~532 eV) and iron-L (~708 eV) core scattering edges from [i] phyllosilicate matrix of band 3, [ii] noncrystalline iron-rich region of band 3 (see Figure 3), and [iii] iron oxide (Fe_3O_4) standard. Specimen thickness was ~500 Å, and the incident electron beam energy was 200 KeV. (B) Selected-area electron diffraction pattern obtained from polycrystalline region of Fe-rich stain. Measured ring spacings correspond to magnetite (Fe_3O_4) ($\lambda CL = 38.8$). (C) A [iii] zone axis microdiffraction pattern obtained from a ~200 Å thick Fe metal crystal in an Fe-rich region of band 3 ($\lambda CL = 36.36$).

basal fringes are aligned approximately parallel to the surface.

The second phase in band 1 was identified as a smectite clay having a basal (001) spacing between 10 and 18 Å. (Smectite rapidly dehydrates during electron irradiation, and the structure collapses accordingly.) Quantitative thin-film analyses indicated that this phase is a nickel-containing saponite. The analytical results for band 1 are shown in Table 3 (all analyses are from

$\rightarrow$

Figure 6. (A) Bright-field electron image of band 4 and segments of bands 3 and 5. Note fibrous microstructure of band 4 relative to bands 3 and 5 which is typical of phyllosilicates. (B) High-resolution lattice-fringe image of band 4 showing an intergrowth of serpentine (7.3-Å basal spacing) and smectite (12-Å basal spacing). During electron irradiation, the smectite degraded more rapidly than the serpentine; hence, its lattice fringes are not as clearly defined. (C) [00l] zone axis microdiffraction pattern obtained from serpentine crystal similar to the one shown in (B). The pattern is indexed in terms of a monoclinic unit cell having lattice parameters of $a = 5.32$, $b = 9.19$, and $c = 14.63$ Å, and $\beta = 93.29°$ (Wicks and O'Hanley, 1988). (D) Bright-field electron image of band 3 in glass II showing inclusions of a U-Ti oxyhydroxide dispersed throughout a phyllosilicate matrix.
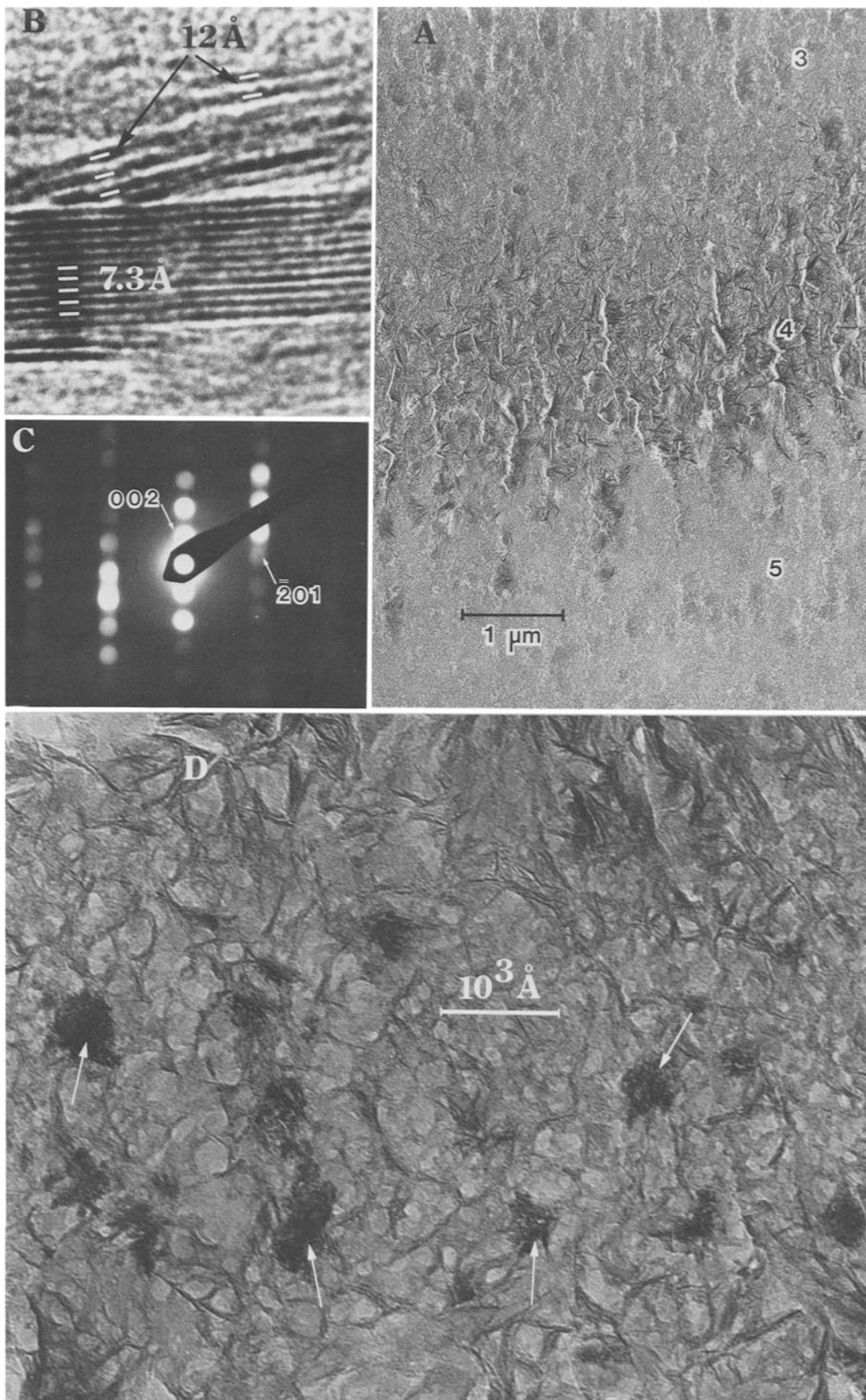
Table 2. X-ray powder diffraction of birnessite.

Birnessite 546D		K-Birnessite[1]	
d	I/I_0	d	I/I_0
6.96	100	7.01	s
3.49	50	3.54	m
		2.54	w
2.47	<1	2.48	w
2.42	10	2.41	w
		2.26	w
2.14	25	2.12	w
1.85	5		
1.80	5		
1.51	<1		
1.46	<1		
1.43	<1		
1.24	<1		

[1] Golden *et al.* (1986). s = strong; m = medium; w = weak.

Table 3. Quantitative thin-film X-ray analyses of bands of sample 546D.[1]

Band	Element (atom %)							
	Mg	Al	Si	Ca	Ti	Mn	Fe	Ni
1	20.5	10.0	38.2	0.4	1.1	23.9	0.3	6.3
2	22.7	14.3	44.3	0.2	—	6.9	3.2	9.2
3	4.4	7.1	56.8	1.0	1.7	4.0	20.5	4.5
4	9.9	8.9	51.7	0.8	1.0	1.9	17.9	8.0
5	—	5.3	61.0	1.1	1.2	1.8	25.7	2.2
6	1.1	9.4	63.3	3.1	1.5	1.4	16.4	3.0

[1] Atom abundance determined using the thin-film procedure of Cliff and Lorimer (1975). The reported composition represents an average composition as determined by replicate analyses of each layer.

sample 546D) and suggest a mixture of birnessite and smectite. The composition of the smectite was determined by assuming that all of the Mn present was due to a Ni-containing birnessite, and the remainder was attributed to smectite. If all of the Fe is assumed to be in the ferric state (based on its coexistence with birnessite), the following approximate structural formula for sample 546D can be calculated on an 11-oxygen equivalent basis: $Ca_{0.03}(Mg_{1.92}Ti_{0.10}Fe^{3+}{}_{0.03}Ni_{0.23}Al_{0.52})$-$(Si_{3.58}Al_{0.42})O_{10}(OH)_2$.

Band 2. Band 2 is a thin continuous region beneath band 1 in all samples. It consists of fibers oriented perpendicular to the surface (Figure 3). AEM analyses indicate that band 2 is composed mostly of saponite intermixed with minor amounts of fibrous birnessite (Table 3). Band 2 became progressively more saponite-rich and well ordered as the reaction time increased, although the thickness of the band changed little. The composition of the smectite in band 2 closely matches that in band 1, based on the same assumptions that were used for band 1, and the calculated approximate structural formula for sample 546D is $Ca_{0.01}(Mg_{1.71}$-$Fe^{3+}{}_{0.24}Ni_{0.61}Al_{0.42})(Si_{3.34}Al_{0.66})O_{10}(OH)_2$.

Band 3. Band 3 is a complex mixture of noncrystalline and poorly crystalline phases intergrown on a scale of a few hundred Ångstroms. Because of such fine-scale heterogeneity, phase identifications were inferred from the combination of bulk thin-film analyses, lattice images, and, where possible, electron microdiffraction patterns. Nanometer-size crystallites having basal spacings of 10–12, 7.3, and 6.9 Å were observed, suggesting the coexistence of smectite, birnessite, and a 7.3-Å phase. On the basis of results obtained from band 4 (see below), the 7.3-Å phase is probably serpentine. The bulk thin-film data (Table 3) are also consistent with a mixture of these phases containing a dominant silicate (Fe-rich smectite and/or serpentine) component and minor birnessite. Because the ratio of the

three phases throughout band 3 varied with proximity to bands 2 and 4, the actual composition of the phases could not be determined solely from the data from band 3. These phases are discussed further with band 4.

Band 3 also contains lenses of Fe-rich material (see Figures 2C and 3B). In samples 195D and 546D, these lenses are noncrystalline, but in samples 14D and 28D, they are partially ordered. The lenses are located at the interface between bands 2 and 3 and also penetrate into band 3. Magnetite and metallic Fe were identified in the lenses by electron energy-loss near-edge structure (ELNES) (Figure 5A) and electron diffraction (Figures 4B and 5C). ELNES is a method that is useful for empirically studying atomic arrangements (e.g., coordination and oxidation states) that are difficult to study by other electron beam techniques (see Tafto and Zhu, 1982; Egerton, 1986). Figure 5A shows an example of ELNES applied to the Fe-rich lenses in band 3: the iron-L edges show little change in near-edge structure from [i] through [iii], but the oxygen-K edges show significant variation. Comparison of the O-K edge structure of [i] and [ii] indicates that the environment of the oxygen differs between the phyllosilicate and the region of the noncrystalline iron-rich stain. Comparison of [ii] and [iii] suggests that the noncrystalline stain is an iron oxide because the O-K edge structure in [ii] is very similar to that of the oxide in [iii]. The presence of reduced iron (Figure 5C) in a system that appears to be oxidizing is surprising, inasmuch as care was taken to use low irradiation intensities so that the possibility of Fe reduction in the electron beam was minimized. In fact, no differences in diffraction characteristics were observed, even after extended monitoring of Fe sites in either the noncrystalline or crystalline materials.

Band 4. Band 4 contains the most well-ordered material in the altered glass (Figure 6), with the exception of birnessite crystals (Figure 4). This band is present in samples 195D and 546D but not in samples 14D and 28D. At least two phyllosilicates were found in-
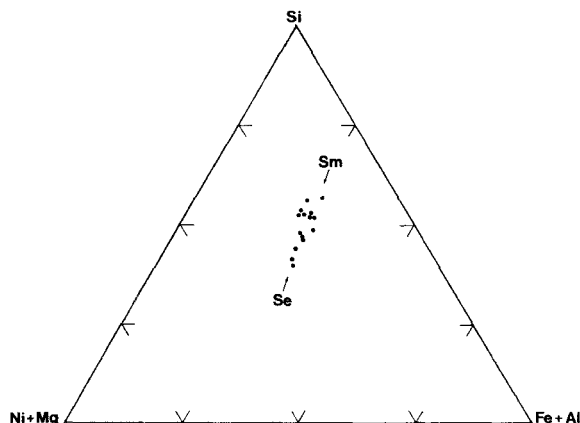
Figure 7. (Mg + Ni) − Si − (Fe + Al) ternary composition plot of 15 quantitative point-count analyses obtained from band 4. Element concentrations are expressed as atom abundances. Distribution of data points suggests smectite (Sm) and serpentine (Se) intimately ingrown on a nanometer scale. Serpentine-rich area (lower data points) is slightly enriched in Mg and Ni relative to smectite (upper data points).

tergrown on a nanometer scale (Figure 6B). Lattice-fringe images indicated basal spacings of about 7 Å and ranging between 10 and 12 Å. Electron microdiffraction patterns (e.g., Figure 6C) confirmed that two phyllosilicates having basal spacings of 7.3 and 12 Å were present in band 4, and that the two-dimensional symmetry of these patterns was consistent with serpentine and smectite, respectively.

Figure 7 shows a ternary composition plot of quantitative thin-film analyses of band 4. The X-ray spatial resolution of each analysis was estimated to be >500 Å. Near end-member compositions (i.e., lowermost and uppermost data points) are consistent with serpentine and smectite, respectively. Figure 7 indicates that the serpentine phase contained significantly more Mg and Ni than the smectite. Based upon nanoprobe analysis of the 12-Å phase, an approximate structural formula of $M^+(Mg_{0.75}Fe^{2+}_{1.25}Ni_{0.39}Al_{0.46})(Si_{3.85}Al_{0.15})O_{10}(OH)_2$ was obtained. A small amount of Ca was also detected, but a quantitative estimate could not be made. Because the smectite is very iron rich, all the iron was considered as ferrous to derive a consistent structural formula. This assignment is consistent with the observation of magnetite and metallic Fe nearby in band 3.

Bands 5 and 6. Bands 5 and 6 show the least extent of crystallization in the altered regions, with band 6 exhibiting a degree of order similar to that of the unreacted glass. Although band 5 was noted in all samples, band 6 was found only in samples 195D and 546D. Band 5 contains some regions of ordered material; isolated serpentine and/or smectite stringers of band 4 have penetrated into band 5 to a depth of 2–4 μm, and rare, nanometer-size crystallites are randomly distributed. The latter crystallites may have been smec-
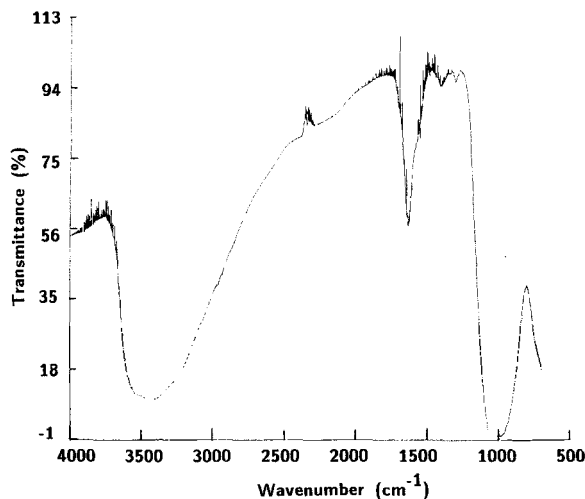

Figure 8. Infrared spectrum of replicated reaction region (bands 3 and 5) from sample 28D.

tite, inasmuch as they exhibit a 12-Å basal spacing. Compared to bands 3 and 4, band 5 is depleted in Mg, Al, and Ni and has a lower cation-to-silicon ratio (Table 3). Based on a total weight percent analysis of band 5, about 35% of the band can be attributed to molecular water or hydroxyl. This is the largest concentration of water in any of the bands; as a result, the band structure is punctuated with large cracks oriented perpendicular to the layering. These cracks were probably formed during storage of the samples prior to analysis and during beam irradiation, and were confined mainly to band 5.

Transmission IR spectra were collected on bands 3 and 5 that were carefully peeled from sample 28D (Figure 8). Three absorption bands (1040, 1650, and 3500 cm^{-1}) are predominate in the spectra, along with an increase in absorption starting at 600 cm^{-1}. The bands at 1040 and 600 cm^{-1} are related to Si–O-stretching modes of the silicate structure, the 3500 cm^{-1} band is attributed to the OH-stretching mode of molecular water and hydroxyl, and the 1650 cm^{-1} band is due to the scissor-bending mode of molecular water. The ratio of molecular water to hydroxyl was determined from the molar absorptivity values published by Newman *et al.* (1986) and yielded a molecular water/hydroxyl ratio of ~3.5. Hence, molecular water appears to be the dominant species in bands 3 and 5, which are the main bands in sample 28D.

Band 6 shows no evidence of structural order. The composition varies but is generally intermediate between the unaltered glass and band 5. The composition of band 6, near its interface with the unaltered glass, resembles that of the unaltered glass except for the almost complete removal of Na, Li, and B, as determined by electron and ion-beam profiling (Figure 9).

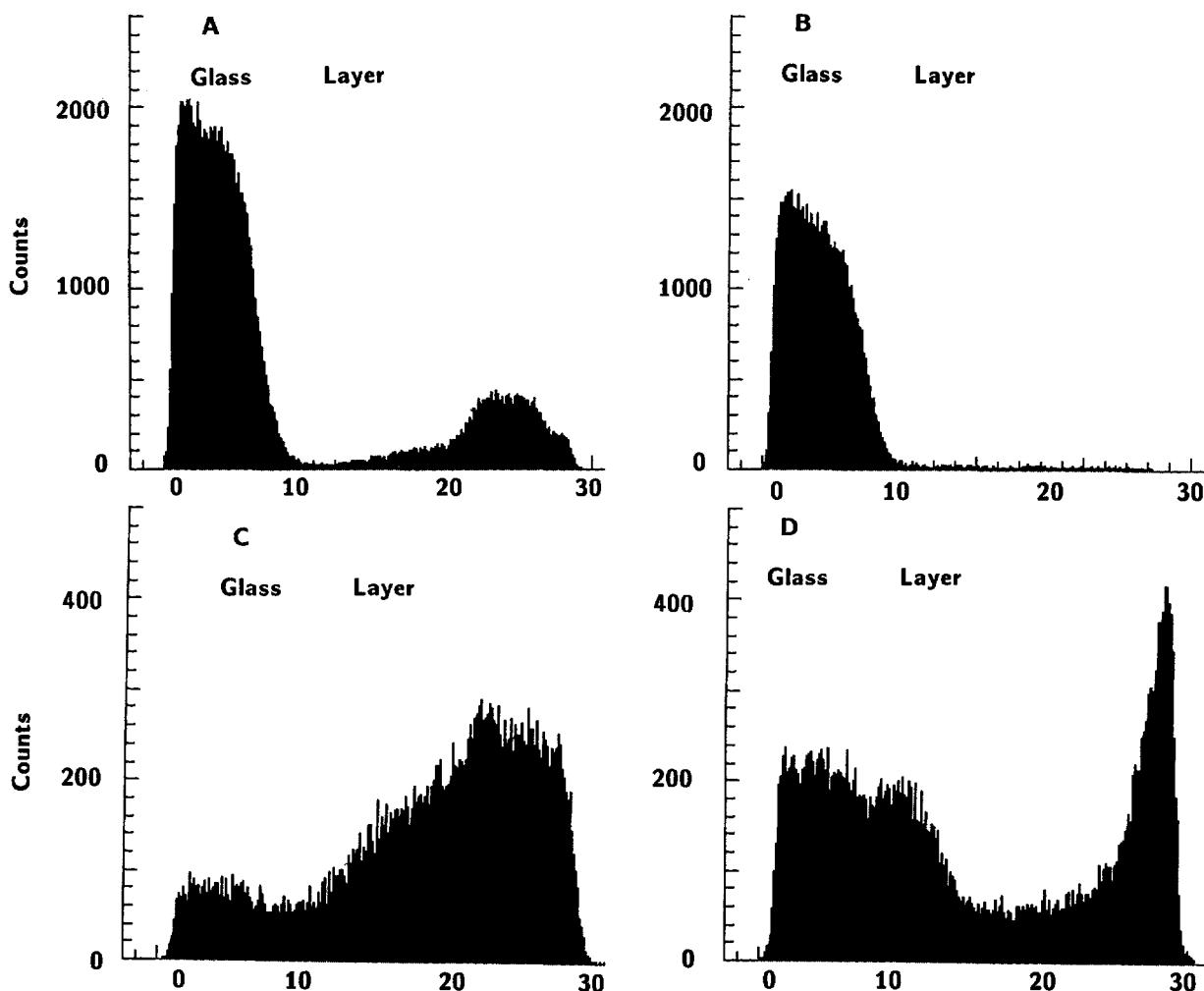Cross sections of the six bands shown in Figure 1

Figure 9. Ion-beam profiles across reacted regions of sample 546D. (A) Li, (B) B, (C) Mn, and (D) Nd. The y axis is ion intensity in number of counts; the x axis is thickness in μm.

were examined with ion-microprobe imaging (IMI). Of particular interest is the distribution of elements that could not be readily resolved with electron beam techniques, e.g., Ce, Nd, and La. Elemental profiles across the reacted region were obtained by selectively displaying elemental ion intensities along a straight path from the glass through the bands. The spatial resolution for any point on the line profile was estimated to be ~4 μm and was limited due to sputtering and sample-charging artifacts. Because the entire reacted region on sample 546D was ~30 μm thick, general element distribution information could be obtained.

Selected ion-microprobe elemental profiles are shown in Figure 9. The glass-band 6 interface is marked by a sharp depletion of B and Li, whereas Mn shows a marked increase in bands 1 and 2. The rare earth elements all show similar profiles, as represented by Nd in Figure 9D. The rare earth intensity gradually in-

creases from band 5 to 3, with a slight maximum near the boundary between bands 3 and 4. These profiles suggest that rare earth elements did not selectively partition into one particular mineral phase, nor did they precipitate at the surface as did Mn, Ni, and Ba.

Glass II

Understanding the behavior of radionuclides is important for determining the long-term suitability of glass as a waste form. Sample 1280D (glass II) was examined with particular emphasis on the distribution of uranium within the reaction bands. The leachate results indicate that uranium was released from glass II at a rate 7 to 20 times less than that for boron, depending on the leaching time. This result is surprising considering previously observed uranium release trends, in which boron and uranium were released to the solution according to their stoichiometric propor-

tions in the glass (Ebert *et al.*, 1990). The solution data from the present tests suggest that uranium was preferentially retained in the glass.

As shown in Figure 6D, inclusions of a uranium-titanium-oxygen-bearing phase are present in the reacted layers. Because these inclusions are poorly crystallized aggregates of nanometer-sized grains, no definitive crystal structure data could be obtained.

DISCUSSION

Origin of reacted layers

The morphology, microstructure, and composition of the bands and their evolution as a function of reaction progress are the most direct clues to their origin (Figures 1–3). An overview of the degree of structural order and crystallinity for the sequence of bands is shown in Figures 10 and 11. A clear trend can be seen toward more order and crystallinity as a function of both time and sequence in which the bands form. The birnessite and smectite particles in band 1 occur as highly porous islands above the original glass surface (in contrast to the compact structures of the underlying subsurface bands); this suggests that band 1 precipitated from the leachate. The saponite in band 2 is oriented perpendicular to the surface, reminiscent of secondary phase textures seen in natural water-rock systems (Wilson and Pittman, 1977). Band 2 probably formed at the original glass surface prior to deposition of band 1 (Figure 3A). This observation, together with its near monomineralic composition, strongly suggests that band 2 grew into the aqueous solution phase during the earliest stages of alteration.

Morphologically, bands 3 through 6 have characteristics similar to those of the original glass. For example, Fe-rich regions (Figures 1–3) form a continuous pattern tracing the solution side of band 3. These Fe-rich regions also penetrate into band 3, following microcracks present in the original glass surface (Figure 1). The continuous Fe-rich pattern demarcates the outermost limit of the original glass. Bands 3–6 were noted on the glass side of the continuous Fe-rich pattern and formed as the glass restructured. Because of this *in situ* transformation, the bands are residual in nature. The compositions of the residual bands 3 to 6 are consistent with a leached glass origin (Doremus, 1973); however, bands 3–5 contain crystalline materials whose compositions strongly reflect that of the residual host. For example, where the Fe/Mg ratio in the band is high, the Fe/Mg ratio of the smectite is correspondingly high. These observations indicate that the crystalline phases observed in bands 3 through 5, including the U-Ti-O phase, must have nucleated *in situ*. From the SEM and AEM analyses, bands 3 through 6 clearly grew inward into the glass. This inward reaction progress is to be expected because hydrolysis reactions between water and the unaltered glass take place at progressively greater
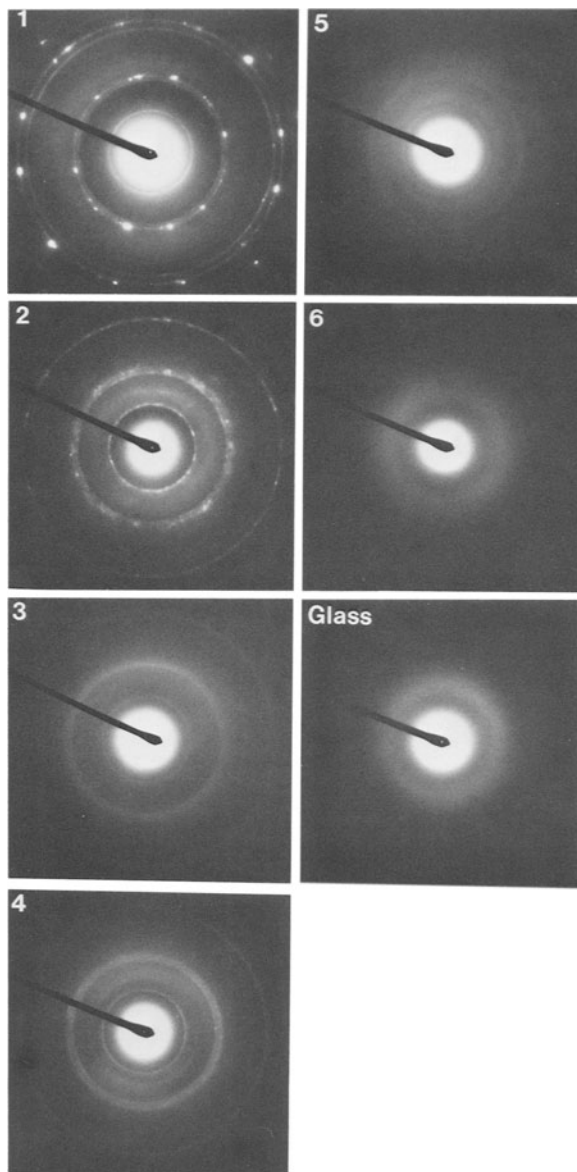

Figure 10.   Selected-area electron diffraction patterns showing changes in degree of structural order within various bands. With the exception of band 4, structural order progressively decreases from band 1 to band 6. Strong spots in band 1 are due to birnessite crystals. Band 2 is dominated by well-ordered saponite, while band 3 contains extremely fine-grained phyllosilicate (probably nontronite). Band 4 contains well-ordered serpentine mixed with smectite, whereas band 5 is compositionally and structurally similar to band 3. Band 6 is structurally similar to the unreacted glass.

depth with increasing reaction duration. Quantitative modeling of the glass reaction process using the geochemical code EQ3/6, combined with mechanistic interpretation of the temporal trends as described above, can be used to predict long-term performance of the glass (Bourcier *et al.*, 1990).
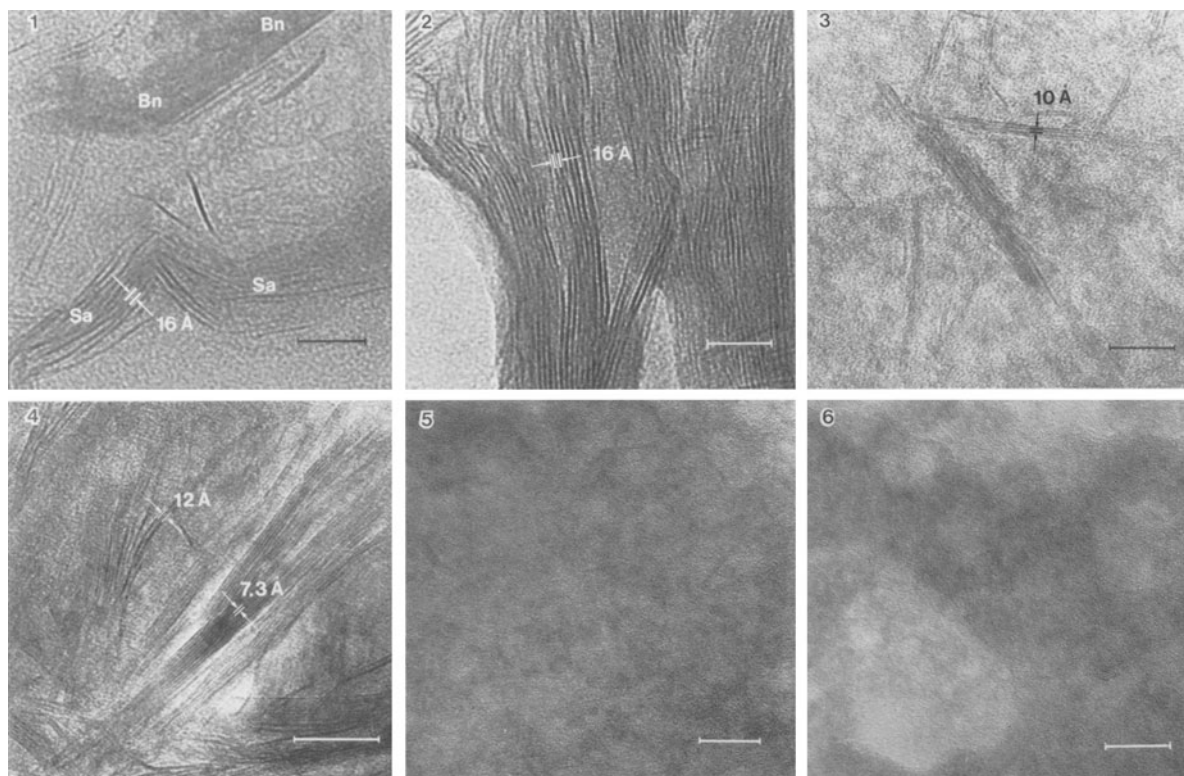
Figure 11. High-resolution lattice-fringe images of phyllosilicates in bands 1 through 6. Band 1 contains saponite (Sa) intermixed with birnessite (Bn), band 2 contains predominantly saponite (16-Å basal spacing), band 3 contains Fe-rich smectite (~10-Å basal spacing), and band 4 is a mixture of smectite and serpentine (with basal spacings of 12 and 7.3 Å, respectively). Band 5 is disordered with only rare nanometer-scale regions of order. Band 6 has a degree of order similar to that of the unreacted glass.

Implications to nuclear waste disposal

Licensing of a high-level nuclear waste repository will require development of a performance model that predicts the long-term stability of waste glass and describes the fate of radionuclides in the storage environment. The formation of an actinide-bearing secondary phase within the reacted bands and the segregation of rare earth elements between bands are significant because they reveal that radionuclide release could be retarded even though the glass continues to react. In this regard, the observation of birnessite and a U-Ti-O phase within the alteration bands of glasses I and II is interesting. Birnessite exhibits a strong ion-exchange preference for heavy metals (Giovanoli *et al.*, 1970) and can be converted to hollandite by heating. Hollandites have been used as a radionuclide-bearing phase in the synthetic waste form SYNROC (Ringwood and Kesson, 1988; Giovanoli *et al.*, 1970; Giovanoli and Balmer, 1981). The lack of uranium or rare earth uptake by precipitated birnessite in glass II, however, along with the appearance of the U-Ti-O phase, suggests that the formation of a stable actinide phase rather than ion exchange may be the primary mechanism for retarding radionuclide release into the environment. The systematics of actinide phase formation during glass leaching and the role of existing cations (e.g., titanium) are fertile areas of future research.

ACKNOWLEDGMENTS

REFERENCES

Abrajano, T. A., Jr., Bates, J. K., Gerding, T. J., and Ebert, W. L. (1988) The reaction of glass in a gamma irradiated saturated tuff environment, Part 3: Long-term experiments at 1×10^4 rad/hour: *Argonne Natl. Lab. Rept.* **ANL-88-14,** 1–117.

Abrajano, T. A., Jr., Bates, J. K., and Bradley, J. P. (1989) Analytical electron microscopy of leached nuclear waste glasses: in *Ceramic Transactions, Vol. 9, Nuclear Waste*

Management III, G. Mellinger, ed., American Ceramic Society, Westerville, Ohio (in press).

Bates, J. K., Lam, D. J., and Steindler, M. J. (1983) Extended leach studies of actinide doped SRL 131 glass: in *Scientific Basis for Nuclear Waste Management VI,* D. G. Brookins, ed., North-Holland, New York, 183–190.

Bourcier, W. L. (1989) Geochemical modeling of radioactive waste glass: *Lawrence Livermore Natl. Lab. Rept.* **UCRL-57012,** 1–7.

Bourcier, W. L., Peiffer, D. W., Knauss, K. G., McKeegan, K. D., and Smith, D. K. (1990) A kinetic model for borosilicate glass dissolution based on dissolution affinity of a surface alteration layer: in *Scientific Basis for Nuclear Waste Management XIII,* V. Oversby and P. Brown, eds., Materials Research Society, Pittsburgh, 209–216.

Bradley, J. P. (1988) Analysis of chondritic interplanetary dust thin sections: *Geochim. Cosmochim. Acta* **52,** 889–900.

Bradley, J. P. and Brownlee, D. E. (1989) Cometary particles: Thin sectioning and electron beam analysis: *Science* **231,** 1542–1544.

Bradley, J. P., Germani, M. S., and Brownlee, D. E. (1989) Automated thin-film analysis of anhydrous interplanetary dust particles in the analytical electron microscope: *Earth Planet. Sci. Lett.* **93,** 1–13.

Chen, C. C., Golden, D. C., and Dixon, J. B. (1986) Transformation of synthetic birnessite to cryptomelane: An electron microscope study: *Clays & Clay Minerals* **34,** 565–571.

Cliff, G. and Lorimer, G. W. (1975) The quantitative analysis of thin sections: *J. Microsc.* **103,** 203–207.

DOE (1989) Site characterization plan, Yucca Mountain Site: Nevada Research and Development Area, *U.S. Dept. of Energy Rept.* **DOE/RW-0199,** 7.1–8.7.

Doremus, R. H. (1973) *Glass Science:* Wiley, New York, 76–92.

Ebert, W. L., Bates, J. K., and Gerding, T. J. (1990) The reaction of glass during gamma irradiation in a saturated tuff environment, Part 4: SRL 165, ATM-1c, and ATM-8 glasses at 1E3 R/h and 0 R/h: *Argonne Natl. Lab. Rept.* **ANL-90/13,** 5–17.

Egerton, R. R. (1986) *Electron Energy-Loss Spectroscopy in the Electron Microscope:* Plenum Press, New York, 410 pp.

Giovanoli, R. and Balmer, B. (1981) A new synthesis of hollandite. A possibility for immobilization of nuclear waste: *Chima* **35,** 53–55.

Giovanoli, R., Stahli, E., and Feitkuecht, W. (1970) Über Oxihydroxide des vierwertigen Mangans mit Schichtengitter 1. Natrium-Mangan(II,III) Manganat(IV): *Helv. Chim. Acta* **53,** 209–215.

Golden, D. C., Dixon, J. B., and Chen, C. C. (1986) Ion exchange thermal transformations and oxidizing properties of birnessite: *Clays & Clay Minerals* **34,** 511–520.

Godon, N., Thomassin, J., Touray, J., and Vernaz, E. (1988) Experimental alteration of R7T7 nuclear model glass in solutions with different salinities (90°C, 1 bar): Implications for the selection of geological repositories: *J. Mat. Sci.* **23,** 126–132.

Grambow, B. (1985) A general rate equation for nuclear waste glass corrosion: in *Scientific Basis for Nuclear Waste Management VIII,* C. M. Jantzen, J. A. Stone, and R. C. Ewing, eds., Materials Research Society, Pittsburgh, 15–27.

Lutze, W., Malow, G., and Rabe, H. (1983) Surface layer formation on a nuclear waste glass: in *Scientific Basis for Nuclear Waste Management VI,* D. G. Brookins, ed., North-Holland, New York, 37–45.

Mendel, J. E. (1984) Final report of the defense high level waste leaching mechanisms program: *Battelle Pacific Northwest Lab. Rept.* **PNL-5157,** 1.1–1.63.

Murakami, T., Bamba, T., Jercinovic, M., and Ewing, R. (1989) Formation and evolution of alteration layers on borosilicate and basalt glasses: Initial stage: in *Scientific Basis for Nuclear Waste Management XII,* W. Lutze and R. Ewing, eds., Materials Research Society, Pittsburgh, 65–72.

Newman, S., Stolper, E. M., and Epstein, S. (1986) Measurement of water in rhyolitic glasses: Calibration of an infrared spectroscopic technique: *Amer. Mineral.* **71,** 1527–1541.

Ringwood, A. E. and Kesson, S. E. (1988) SYNROC: in *Radioactive Waste Forms for the Future,* North-Holland, New York, 156–177.

Sheridan, P. (1989) Determination of experimental and theoretical KAS: Factors for a 200 keV analytical electron microscope: *J. Electron Microsc. Tech.* **11,** 41–61.

Slate, S. C. (1985) Standardized waste form test methods: in *Scientific Basis for Nuclear Waste Management VIII,* C. Jantzen, J. Stone, and R. Ewing, eds., Materials Research Society, Pittsburgh, 741–746.

Tafto, J. and Zhu, J. (1982) Electron energy loss near edge structure (ELNES), a potential technique in the studies of local atomic arrangements: *Ultramicroscopy* **9,** 349–454.

Wicks, F. G., and O'Hanley, D. S. (1988) Serpentine minerals: Structures and petrology: in *Hydrous Phyllosilicates (Exclusive of Micas), Reviews in Mineralogy, Vol. 19,* S. W. Bailey, ed., Mineralogical Society of America, Washington, D.C., 91–167.

Wicks, G. G., Stone, J. A., Chandler, G. T., and Williams, S. (1986) Long-term leaching behavior of simulated, Savannah River Plant waste glass: E.I. du Pont de Nemours Co., *Savannah River Lab. Rept.* **DP-1728,** 1–37.

Wilson, M. D. and Pittman, E. D. (1977) Authigenic clays in sandstones: Recognition and influence of reservoir properties and Paleoenvironmental analysis: *J. Sed. Pet.* **47,** 3–31.